Spatiotemporal optimization on cross correlation for particle image velocimetry ⊘

Zongming Xie (谢宗明) ; Hongping Wang (王洪平) ; Duo Xu (徐多) ✉

Check for updates

CrossMark

View Online

Export Citation

Articles You May Be Interested In

Control reattachment of backward-facing step flow using a row of mini-jets in recirculation bubble

Physics of Fluids (August 2022)

Measurement of bubbly flow using spatiotemporal filter velocimetry coupled with molecular tagging

AIP Conference Proceedings (April 2014)

Investigating flow patterns and related dynamics in multi-instability turbulent plasmas using a three-point cross-phase time delay estimation velocimetry scheme

Physics of Plasmas (April 2016)
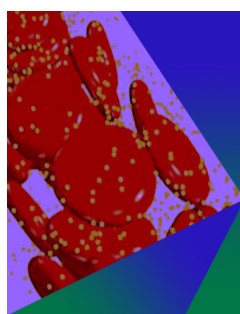
Physics of Fluids

Special Topic: Flow and Forensics

Submit Today!

AIP Publishing

Spatiotemporal optimization on cross correlation for particle image velocimetry

View Online   Export Citation   CrossMark

Zongming Xie (谢宗明),[1] (iD) Hongping Wang (王洪平),[1,2] (iD) and Duo Xu (徐多)[1,2,a] (iD)

AFFILIATIONS

[1]The State Key Laboratory of Nonlinear Mechanics, Institute of Mechanics, Chinese Academy of Sciences, Beijing 100190, China
[2]School of Engineering Science, University of Chinese Academy of Sciences, Beijing 100049, China

[a]Author to whom correspondence should be addressed: duo.xu@imech.ac.cn

ABSTRACT

We introduce an optimization method for the cross-correlation operation in particle image velocimetry by locating the correlation peaks assisted with constraint conditions. In this study, an objective function was constructed to include the residual of the normalized cross-correlation term, a component in charge of spatial smoothness (inspired by the optical flow method as used in a previous study) and a component for temporal smoothness (inspired by the concept of trajectory selection in particle tracking velocimetry). Minimizing the objective function gives optimized velocity fields for a series of tracer images for spatiotemporal smoothness. The proposed method was examined in synthetic images of turbulent flow and Batchelor vortex and in a laboratory experiment of vortex rings. The effect of image background noises and the initial guess for the optimization process were examined and discussed.

Published under an exclusive license by AIP Publishing. https://doi.org/10.1063/5.0091839

I. INTRODUCTION

Further understanding of flow physics in experiments is largely facilitated by the development of measurement techniques. It is particularly the case for measurement techniques of velocity, given that which is a key variable from the perspective of Navier–Stokes equations. Particle image velocimetry (PIV), a non-intrusive measurement technique of flow velocity, provides substantial measurement progress in revealing insights into varieties of fluid flows (Adrian, 1991). In standard planar PIV experiments, neutrally buoyant small-sized tracer particles uniformly seeded in a flow are illuminated by a laser sheet. Given that fluid motion is approximately represented by the particle motion by neglecting the particle-flow slipping effect, the calculation of the particle motions recorded in particle images gives the flow field (Westerweel, 1997). The cross correlation method is robust and usually applied to obtain the particle displacement in each interrogation window of the particle images, and a vector for an interrogation window corresponds to the most probable motion of a few particles in this window (Raffel *et al.*, 2018). The large size of the interrogation window brings in coarse spatial resolution of the PIV measurements (missing revealing small flow structures smaller than the window), while the small size of the window leads to more of the miss-paired particles (resulting in low signal-to-noise on the correlation mapping). Balancing the effects of the large and small window sizes gives a typical window size of about 32×32 pixels^2 to reach the typical uncertainty of about 0.1 pixel (Raffel *et al.*, 2018).

Studies have been performed to improve the spatial resolution of the PIV measurements while maintaining the measurement precision, e.g., Keane *et al.* (1995) proposed a super-resolution method, which combines particle tracking velocimetry (PTV) and PIV. Their local velocity field estimated by the PIV is taken as an input to a PTV process, to obtain the displacements of all individual particles, for improving the spatial resolution of the measurement. Thereafter, particle detection and particle pairing in consecutive frames have been investigated and improved in this hybrid framework (e.g., Cowen and Monismith, 1997; Stitou and Riethmuller, 2001). An iterative multigrid method was introduced to perform progressive grid refinement to increase the spatial resolution, while enhancing the particle–particle matching through the transformation of the interrogation windows (Scarano and Riethmuller, 2000) and iterative image deformation (Scarano and Riethmuller, 2002). Scarano (2004) proposed a super-resolution method, based on the image correlation for the second-order spatial derivatives of the particle displacement fields, which is obtained by maximizing the product of the deformed particle patterns in the images through an optimization process.

Data assimilation and machine learning have been used to improve the resolution of velocity fields, in addition to their successful applications in varieties of flow problems (Liu *et al.*, 2020; Xu *et al.*, 2021; Arzani *et al.*, 2021; Li *et al.*, 2022; Morimoto *et al.*, 2021). Schneiders *et al.* (2017) proposed a data assimilation method, which interpolates scattered particle tracking velocimetry measurements

onto a Cartesian coordinate. Their vorticity field is obtained through iteratively minimizing a designed cost function, to reach the aim of improving the spatial resolution. Deng *et al.* (2019) proposed a super-resolution reconstruction method using a generative adversarial network-based artificial intelligence framework for improvement of the reconstruction accuracy in the turbulent flow field and the measurement spatial resolution. Wang *et al.* (2020) employed a convolutional neural network to improve the prediction and spatial resolution of turbulent velocity fields obtained using PIV. Gao *et al.* (2021) employed a fully convolutional network to optimize a coarse velocity guess for reaching a super-resolution calculation. Recently, Wang *et al.* (2022) applied a physics-informed neural network to reconstruct the dense velocity field from sparse experimental data by minimizing a loss function, which is consisted of the residuals of the data and the Navier–Stokes equations.

Another way of improving the spatial resolution is to impose a constraint condition directly on the cross correlation process. Wang *et al.* (2020) proposed a global optimization (GO) method. This method is based on the cross correlation algorithm with the additional inclusion of the constraint of spatial smoothness inspired by the optical flow method (Liu and Shen, 2008; Liu *et al.*, 2015), through minimizing the objective function consisting of a cross-correlation residual term and a smoothing penalty term. The solution of this objective function gives an optimized vector field with spatial smoothness. This method can employ a very small interrogation window (five pixels) to the densely seeded tracer images to improve the spatial resolution. This global optimization method gives only the spatially optimized result for each time instant. Given the nature of the temporal evolution of the fluid flow (particularly for unsteady flows that are widespread inflow problems), the optimization of the PIV results in both space and time is expected to further improve the measurement quality and suppress the measurement noise. This expectation is inspired by the concept of the Shake-The-Box method in the Lagrangian particle tracking technique (Schanz *et al.*, 2016) that which shakes the reconstructed tracer spatially and constructs a trajectory of the tracer in time. The constraint on both space and time together with the PIV correlation method further improves the PIV measurement accuracy, as demonstrated in this study.

The rest of this paper is organized as follows: In Sec. II, we introduce the present method. In Sec. III, the present method is evaluated through synthetic images. An experiment was carried out to examine the present method in practice in Sec. IV. In Sec. V, we give a discussion on the present method and conclude in Sec. VI.

II. METHODOLOGY

A. Spatiotemporal optimized cross correlation

The method in this study is based on the cross correlation of tracer images. A regularization term, inspired by the optical flow method, is applied to provide a constraint on spatial smoothness over the velocity fields (Wang *et al.*, 2020). The constraint on temporal smoothness is achieved by minimizing the temporal changes of the flow acceleration. This is inspired by the PTV technique that the tracer trajectory, which has the smallest temporal change of the flow acceleration, is taken as the measured trajectory over the candidates (Malik *et al.*, 1993; Xu, 2008). The spatiotemporal optimization (STO) for the cross correlation is achieved by minimizing the residual $R(u, v)$ for each interrogation window,

$$R(u,v) = \int_\Omega \left(\underbrace{[1 - C(u,v)]^2}_{\text{correlation residual}} + \underbrace{\alpha_x^2 (\Delta u)^2 + \alpha_y^2 (\Delta v)^2}_{\text{spatial smoothness}} \right.$$
$$\left. + \underbrace{\beta^2 \left[(\delta a_x)^2 + (\delta a_y)^2 \right]}_{\text{temporal smoothness}} \right) ds. \tag{1}$$

Here, $C(u, v)$ is the correlation map of the displacement $\mathbf{u} = (u, v)$, where u and v correspond to the velocity component along the x and y directions, respectively. $\Delta(\cdot)$ denotes the Laplace operator over the respective velocity component, while $\delta a_{(\cdot)}$ is the temporal change of the flow acceleration component. The flow acceleration $\mathbf{a}$ is obtained by $\mathbf{a} = \partial \mathbf{u}/\partial t + \mathbf{u} \cdot \nabla \mathbf{u}$, where ∇ is the gradient operator and $\mathbf{a} = (a_x, a_y)$ with a_x and a_y being the components along the x and y directions, respectively. Ω is the control domain, while $\alpha_{(\cdot)}$ and $\beta_{(\cdot)}$ are real positive scalars for adjusting the degree of spatial smoothness and temporal smoothness, respectively. For instance, $\alpha_x = \alpha_x^*/\max(|\Delta u|)$ and $\alpha_y = \alpha_y^*/\max(|\Delta v|)$, where α_x^* and α_y^* depend on the window size and are taken the same as Wang *et al.* (2020). Following the analogical way, $\beta = \beta^*/\max(|\delta a|)$ and $0.8 < \beta^* < 1.2$ is found to give close results to the ground truth in our tests (see below) and we use $\beta^* = 1$ in our experimental tests.

In order to minimize the residual R, Eq. (1) is re-written into a linear system. The velocity field is reshaped into a column that u and v take the first and the second halves, respectively. The normalized cross-correlation coefficient is calculated for each interrogation window,

$$C(u,v) = \frac{\sum_{i=1}^{m} \sum_{j=1}^{n} f'(i,j)g'(i+u,j+v)}{\sqrt{\sum_{i=1}^{m} \sum_{j=1}^{n} f'^2(i,j) \sum_{i=1}^{m} \sum_{j=1}^{n} g'^2(i,j)}}, \tag{2}$$

where f' and g' are the paired images by subtraction of the mean gray-scale from the respective tracer images for the interrogation window in size of $m \times n$. The resulted C ranges between -1 and 1. The Laplace operation is performed by the second-order center difference scheme denoted by D_{xx} and D_{yy}, along the x and y directions, respectively. The gradient operation is performed by the center difference scheme, denoted by D_x and D_y along the x and y directions, respectively. The temporal change of flow acceleration δa is calculated by $\delta t \cdot (da/dt)$, where δt is a small time interval and the temporal derivative of the flow acceleration da/dt is calculated using a center difference scheme. For the boundary, a virtual border is implemented in that the value at a grid is set the same as the one of the closest grid at the border.

The residual R is contributed by three components, the correlation residual and the spatial and temporal smoothness of the velocity fields. They compete and are balanced to produce minimized R. Minimizing the residual gives the optimized velocity field with spatial and temporal smoothness.

B. Numerical minimization

The objective function $R(u, v)$ requires to be minimized to give an optimized velocity field. The Levenberg–Marquardt method, in the category of a damped Gauss–Newton method, is used in this study to

solve the nonlinear least-squares problem. For the numerical minimization, a residual column f is constructed,

$$f = \begin{bmatrix} 1 - C(u,v) & \alpha_x(D_{xx}u + D_{yy}u) & \alpha_y(D_{xx}v + D_{yy}v) \\ \beta\delta t(D_{tt}u + uD_tD_xu + vD_tD_yu) \\ \beta\delta t(D_{tt}v + uD_tD_xv + vD_tD_yv) \end{bmatrix}^T, \quad (3)$$

where T denotes the matrix transpose and D_t and D_{tt} are the first-order and second-order temporal gradient operators, respectively. The velocity field has $N(= m \times n)$ velocity vectors, and each component of f has N elements so that f is a vector in dimension $5N \times 1$. This residual f can be minimized with a nonlinear optimization process, and a Newton iteration solver is used in this study. In order to reduce the computation time, a Jacobian matrix of the residual $\mathbf{J} = \partial f / \partial \mathbf{u}$ is derived. (u, v) in $\mathbf{J}$ is updated every step during the optimization iterations (see the explicit matrix form of $\mathbf{J}$ in the Appendix).

The PIV velocity fields at three sequential time instances are required to calculate $\delta \boldsymbol{a}$; thus, these three velocity fields are optimized together while the Jacobian matrix has a size of $11N \times 6N$ to include (u, v) at the three time instants. In principle, velocity fields at more than three time instants can be optimized at the same time, while the size of the Jacobian matrix is correspondingly increased. This may challenge the RAM size of a PC, so in this study, we limit it to three time instants for the concept demonstration.

C. Synthetic images

Two-dimensional synthetic PIV images were rendered and used for examinations of the PIV algorithms, including the classic PIV method, the Global Optimization (GO) method, and the spatiotemporal optimization (STO) method proposed in this study.

A pair of tracer images, obtained at time t_0 and $t_1(= t_0 + \delta t)$, are required for the PIV measurement. At time t_0, several tracers are randomly and homogeneously distributed in the two-dimensional region. The position of a tracer $p(x_0, y_0, t_0)$ is randomly generated, and a unity intensity is set at this position. Then, a Gaussian filtering operation is applied to this tracer so that the intensity at integer grids (pixels) is calculated. A tracer takes about three pixels in diameter (Raffel *et al.*, 2018), and particle density is about 0.05 particles per pixel. This process is repeated for each tracer, after which the intensity of all tracers at the grids is summed up, and is scaled and rounded into a range of 0–240 for an eight-bit image. The velocity of each tracer $\mathbf{u}_p(x_0, y_0, t_0)$ is obtained by interpolation over the numerical data or from the analytical solution. At time t_1, the position of a tracer is obtained by $p(x_1, y_1, t_1) = p(x_0, y_0, t_0) + \mathbf{u}_p(x_0, y_0, t_0)\delta t$. Then, the tracer image is rendered at time t_1 following the steps mentioned above. For rendering sequential tracer images, for each tracer, the position at time t_j is obtained by $p(x_j, y_j, t_j) = p(x_{j-1}, y_{j-1}, t_{j-1}) + \mathbf{u}_p(x_{j-1}, y_{j-1}, t_{j-1})\delta t$, where $\mathbf{u}_p(x_{j-1}, y_{j-1}, t_{j-1})$ is interpolated from the velocity snapshot of the simulation or analytical solution at t_{j-1}.

III. NUMERICAL ASSESSMENT

The introduced method requires examination by comparing results with reference to evaluate its performance. One choice of reference is the velocity data of direct numerical simulation (DNS) of flows, which accurately solves the Navier–Stokes equations without any turbulence modeling. Another option is the flow velocity, which is

specifically designed and generated using analytical formulas. In this study, these two types of numerical assessments are both performed.

A. Direct numerical simulation of forced isotropic turbulence

The velocity data of direct numerical simulation of a three-dimensional forced isotropic turbulent flow are used to evaluate the method introduced in this study. The turbulent flow was carried out in a three-dimensional cube which has periodic boundary conditions along each direction in a Cartesian coordinate, and there are 1024 grid points over 2π long edges along each direction. The Taylor-scale Reynolds number of the flow is 418. The velocity data are online accessible from Johns Hopkins University Turbulence Databases. The velocity data were extracted at the plane $(0 \leqslant x_1 \leqslant \pi, 0 \leqslant x_2 \leqslant \pi, x_3 = \pi)$ over 512×512 grids. Eleven snapshots of the velocity data were downloaded between the time instant of 5 and 6 with a time interval of 0.1 (where the normalization factor of the time scale is not explicitly given in their documentation, and it is usually the viscous time unit). The data were obtained by the sixth order Lagrangian interpolation in space and by the piecewise cubic Hermit interpolation in time.

Four synthetic tracer images (in size of 800×800 pixels^2) were rendered and processed to obtain the velocity fields at three time instants using the three methods. For comparison purposes, the same interrogation window size, 9×9 pixels^2, is used for all three methods, while the distance between the neighboring two vectors is two pixels (giving a window overlap of about 75%). This small interrogation window size (away from the usually used 32×32 pixels^2) is to examine whether they can reach high resolution with an acceptable result. For the classic PIV method, the (FFT) cross-correlation method at a single step (no reduction of the window size at multiple steps) is used. This is also the case for both the global optimization and the present method, before their respective optimization process. This single-step setting holds for all the rest of this paper unless further mentioned.

Figure 1(a) shows the velocity component u of the DNS at times t_1, t_2, and t_3 as the ground truth for reference. The results of the classic PIV method, the global optimization method, and the spatiotemporal optimization method are shown in (b)–(d), respectively. They can capture the main flow structures of the DNS, while missing the very small flow structures. The latter effect is expected since a PIV vector corresponds to the most probable velocity of several tracers in an interrogation window, approximately regarded as a spatial averaging effect over the velocities of the tracers within the window (Xu and Chen, 2013). The difference between the PIV result and the DNS data is not visually clear in Fig. 1 so the measurement error ε quantified by

$$\varepsilon = \left([u - u_{\text{truth}}]^2 + [v - v_{\text{truth}}]^2 \right)^{1/2}, \quad (4)$$

is obtained and shown in Fig. 2, where $(\cdot)_{\text{truth}}$ denotes the respective ground truth from the DNS. The errors of the classic PIV and the global optimization method are slightly larger than that of the spatiotemporal optimization method, given visually that they are slightly darker (for the color legend). For the global optimization and the spatiotemporal optimization method, the error is mainly featured with small structures, which eventually correspond to the small flow structures that cannot be captured by the PIV method (discussed above),
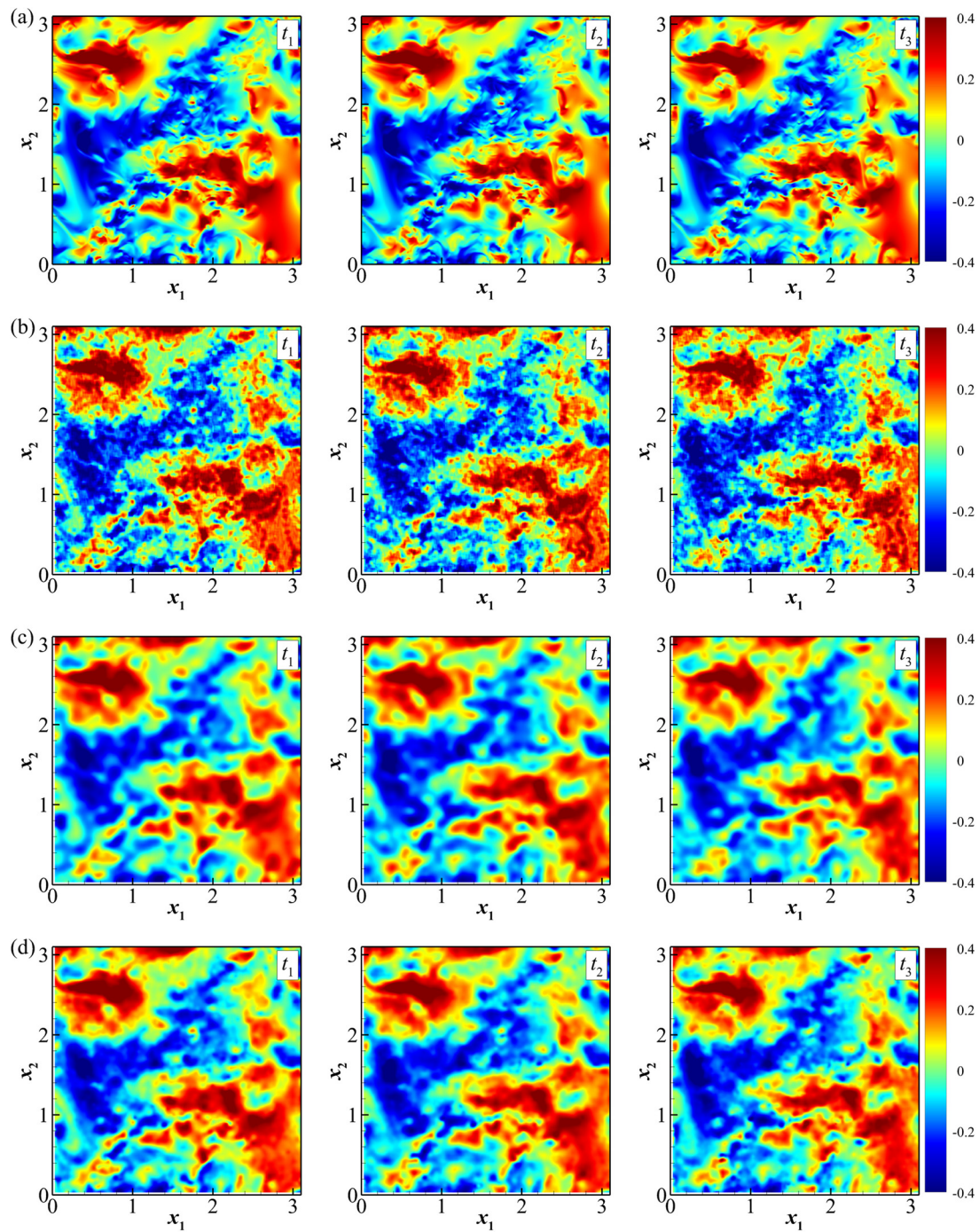
FIG. 1. The color maps of the velocity component u at three time instants (three columns): (a) the DNS data as the ground truth, (b) the classical PIV method, (c) the global optimization PIV method, and (d) the spatiotemporal optimization PIV method.

even if an interrogation window as small as nine pixels in size was used. The probability density function (PDF) of the errors was computed for further quantification. As shown in Fig. 2, the curves of the spatiotemporal optimization method have peaks at $\varepsilon \approx 0.03$–0.04, while the long tails correspond to the relatively larger errors from the small scale structures. The systematic and random velocity errors for all the time instants, quantified by the averaged and standard deviation of the errors, are listed in Table I.
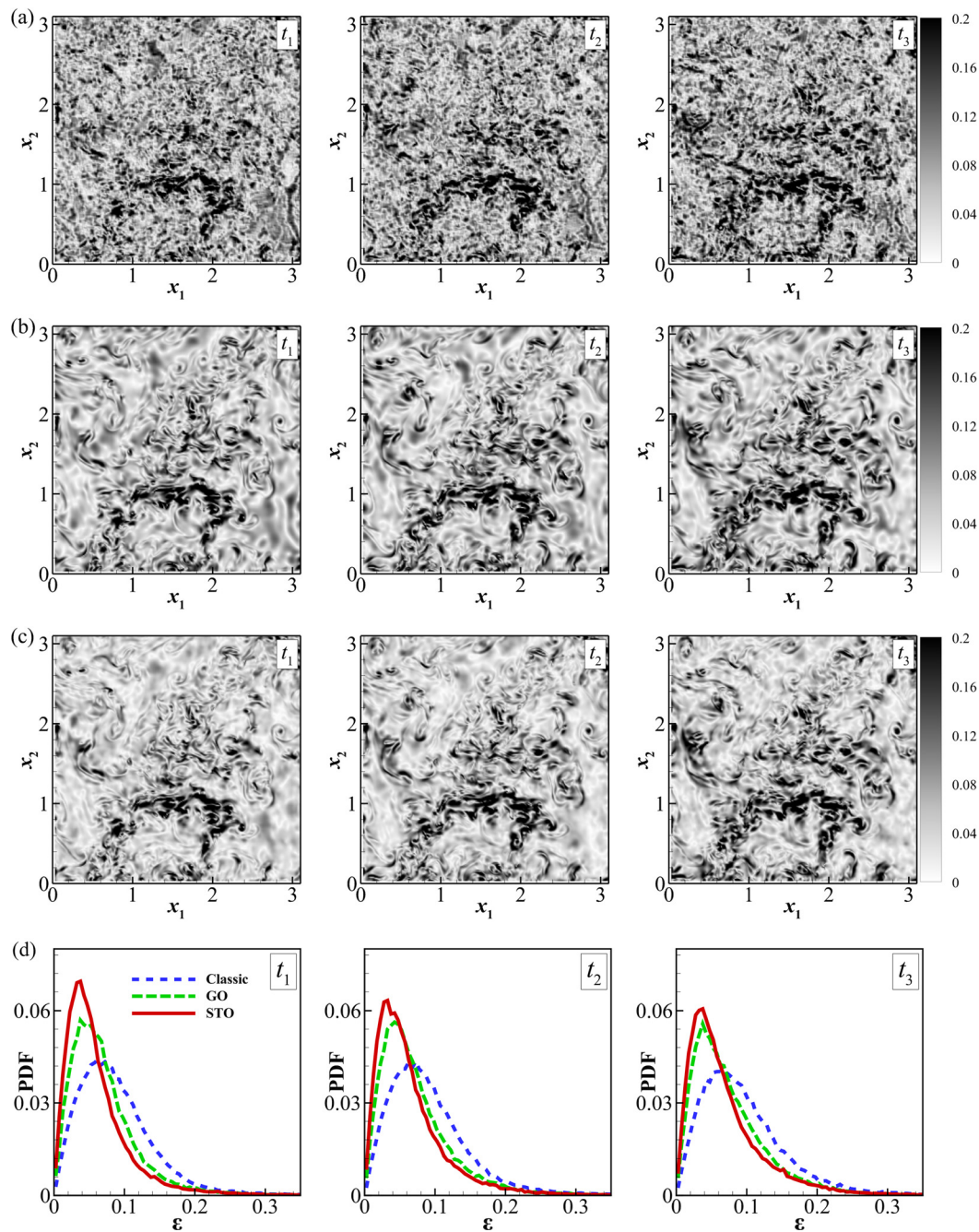
FIG. 2. The contours of the velocity measurement error ϵ at three time instants (three columns): (a) the classical PIV method; (b) the global optimization PIV method; (c) the present (STO) PIV method; and (d) the probability density function (PDF) of the velocity errors, and three panels share the same legend.

B. Batchelor vortex

The typical Batchelor vortex law has a radial velocity of zero, the tangential velocity

$$v_\theta = v_{\theta,\max}(1 + 0.5/\alpha) \times (R/r)\left[1 - \exp(-\alpha r^2/R^2)\right],$$

with

$$\alpha = 1.26, \tag{5}$$

and the axial velocity takes $v_z = v_{z,\max} \cdot \exp(-r^2/R^2)$ (Batchelor, 1964), and r is the radial position. In this study, the vortex core radius is $R = 50$ pixels and the maximum tangential velocity $v_{\theta,\max} = 3$ pixels, the same as Sciacchitano et al. (2012). $v_z = 0$ is used in this study for simplicity and to examine the performance of algorithms on this

TABLE I. The systematic and random errors of the PIV measurements for the forced isotropic turbulence.

	Classic	Global optimization	Spatiotemporal optimization
Systematic error	0.09	0.07	0.05
Random error	0.08	0.07	0.05

TABLE II. The systematic and random errors of the PIV measurements for the Batchelor vortex examination.

	Error type	Classic	Global optimization	Spatiotemporal optimization
$(x_1, x_2)/R \approx (0,0)$	Systematic	0.24	0.16	0.12
$(x_1, x_2)/R \approx (0,0)$	Random	0.091	0.058	0.057
$(x_1, x_2)/R \approx (1,0)$	Systematic	−0.051	−0.0072	0.0092
$(x_1, x_2)/R \approx (1,0)$	Random	0.061	0.039	0.015
All points	Systematic	−0.0012	−0.0082	−0.0026
All points	Random	0.10	0.052	0.025

steady vortex flow. A hundred of synthetic tracer images were generated that the tracers take the Batchelor vortex analogy motions. The synthetic tracer image has a size of 400×400 pixels^2. The interrogation window is 8×8 pixels^2, and the distance between the neighboring two vectors is four pixels (giving a window overlap of about 50%).

Figures 3(a)–3(d) (Multimedia view) show the contours of the tangential velocity v_θ at a time instant, for a visual example. The result of the classic PIV gives rather scattered velocity noise, while the results of the global optimization and the spatiotemporal optimization method are spatially smooth and are visually similar to the analytical velocity. The time series of the tangential velocity v_θ for the three PIV algorithms at the point $(x_1, x_2)/R = (0.02, 0.02) \approx (0,0)$ and $(x_1, x_2)/R = (1.02, 0.02) \approx (1,0)$ are shown in Figs. 3(e) and 3(f). For the vortex center, all three algorithms give large fluctuation measurements. The standard deviation of the fluctuations is taken as the random error, and they range from 0.06 to 0.09, see Table II. The results of the global optimization and the spatiotemporal optimization method are approximately around 0.1, at the bounds of the measurement uncertainty of a standard two-dimensional PIV (0.1 pixel in an optimized configuration), while the results of the classic PIV give a slightly larger deviation from the ground truth. The average of the measurement error (the difference between the measurements and the ground truth), taken as the systematic measurement error, ranges from 0.12 to 0.24. For the point of the maximum tangential speed of

the vortex, the three algorithms give relatively smaller fluctuations that the random error ranges between 0.02 and 0.06 (see Table II). The results of the global optimization and the spatiotemporal optimization method are approximately around 3, and their systematic error is only up to 0.05 in magnitude, which can be approximately bounded by the measurement uncertainty of 0.1 pixel.

IV. EXPERIMENTAL EXAMINATION

The proposed method was examined in a practical laboratory experiment on vortex rings (Glezer, 1988; Gharib *et al.*, 1998; Ma *et al.*, 2022). As shown in Fig. 4, the experiment was carried out in a tank with dimensions of $800 \times 800 \times 800 \, \text{mm}^3$. The tank was made with acrylic plates and was filled with water up to about 750 mm above the bottom of the tank. The vortex rings were generated by a jet flow from an acrylic tube, which has an inner diameter of $D = 40 \, \text{mm}$. The
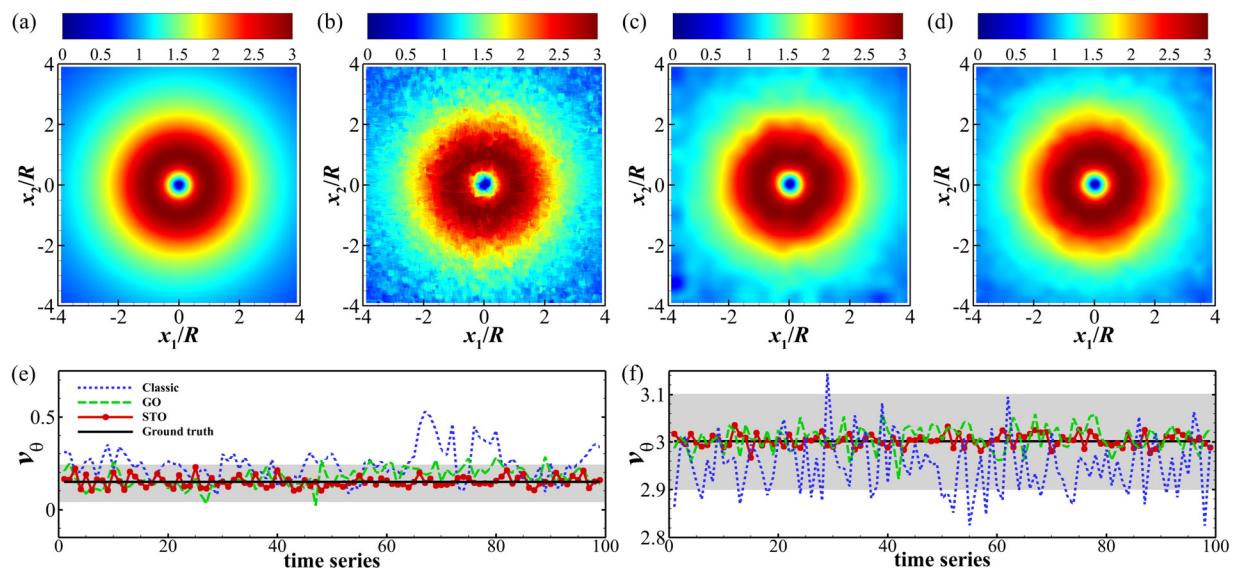

FIG. 3. The contours of the velocity v_θ: (a) the ground truth [Eq. (1)], (b) the classical PIV method, (c) the global optimization PIV method, and (d) the spatiotemporal optimization PIV method. The time series of v_θ at the featured points $(x_1, x_2)/R = (0.02, 0.02) \approx (0,0)$ (e) and $(x_1, x_2)/R = (1.02, 0.02) \approx (1,0)$ (f), which share the same line legend, and the gray area marks the uncertainty band of PIV [0.1 pixel (Raffel *et al.*, 2018)]. Multimedia view: https://doi.org/10.1063/5.0091839.1
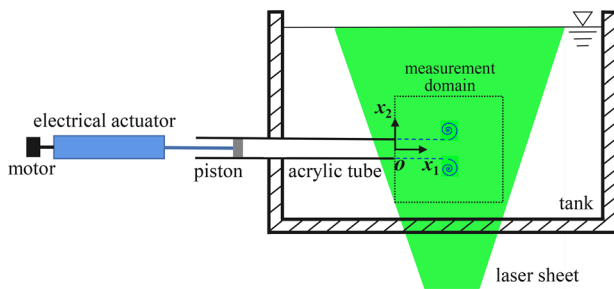
FIG. 4. Schematic diagram of the experimental setup of the vortex ring.

outlet of the tube section is about 240 mm away from the sidewall of the tank and about 275 mm above the bottom of the tank. This section of the acrylic tube was connected to an electrical actuator through a piston, which has an inner diameter of 40 mm. The total length of the tube and the piston is about 2000 mm ($= 50D$). A servo motor equipped with a gearbox was connected to the electrical actuator to control the moving speed of the piston. The rotation of the motor drives the actuator so that the piston pushes the water to flow inside the acrylic tube. A Cartesian coordinate is set with the origin at the center of the tube exit. In this experiment, the Reynolds number $Re = UD/\nu$ is 4000, where ν is the kinematic viscosity of the fluid and $U(=100$ mm/s) is the mean velocity. The motor is rapidly accelerated (within a duration of 10 ms) to the preset speed and runs at this speed constantly until decelerated (within a duration of 10 ms) to a full stop. The stroke of the piston is approximately 10D, which produces a vortex ring without the scenario of pinching off from the jet (Gharib *et al.*, 1998).

To carry out the PIV measurements, the water is uniformly seeded with hollow glass spheres with a diameter of about 11 μm (Raffel *et al.*, 2018). A laser sheet with a thickness of about 1 mm was generated through a group of lenses and mirrors from a continuous laser (10 W). The laser sheet illuminates the middle plane of the tube exit from the bottom of the tank and covers about 160×160 mm^2 as indicated by the green area in the sketch. The PIV images were recorded by a high-speed CMOS camera with a sampling frequency of 100 Hz, which gives the inter-frame time of 10 ms. The maximum particle displacement between adjacent snapshots is about 6–8 pixels. For the interrogation window of 32×32 pixels^2 (as used in the classic PIV configuration), there are approximately five to six tracers. The minimum grayscale value for the time series of the PIV images was taken as the background and subtracted from the raw PIV image before the cross-correlation operation.

The time series of the PIV images were processed by both the classic PIV algorithm and the present method. For the classic PIV method, the iteration algorithm with the interrogation window reduction to the final window size is 32×32 pixels^2 with a 50% overlap (Raffel *et al.*, 2018). For the spatiotemporal optimization PIV method, the same sizes of the interrogation window were used for comparison purposes. No post-processing was applied to the PIV vector fields for the three methods.

The vorticity fields were calculated by the finite-difference scheme and normalized by U/D for the results of both methods, and they are shown in Fig. 5 (Multimedia view) for three time instants. For the vorticity fields of the classic PIV method (a), (e), and (i), the window size of 32×32 pixels^2 (including about five to six tracers) is close to the optimized configuration as suggested by Raffel *et al.* (2018).

The respective results capture the vortex motions well. For the global optimization method, smaller vortex structures can be observed, particularly in panels (e) and (h). For the present method, the vortex structures generally agree with those of the classic PIV and the global optimization. The difference between the present method to the global optimization method is that a few tiny areas with large vorticity are suppressed.

V. DISCUSSION ON THE OPTIMIZATION METHOD
A. Effect of background noise

The examinations above are from approximately ideal images; however, in practice, the images are of background noises caused by, i.e., the dark electrical current in digital imaging sensors and/or scattered light in densely seeded flows. The effect of the image background noise on the PIV results for the proposed method was investigated. One hundred synthetic tracer images were superimposed with the randomly generated normal-distributed noise (Raffel *et al.*, 2018). Then, the contaminated images were processed by the PIV algorithms following the same procedure above. The noise level (grayscale) was controlled and quantified by the signal-to-noise ratio, SNR $= \sigma_{I_0}/\sigma_{I_n}$, where σ_{I_0} and σ_{I_n} are the intensity standard deviation of noise-free images and noise level standard deviation, respectively.

The PIV results from the noise contaminated images are shown in Fig. 6. As the noise level is increased (decreased in SNR), the PIV results deviate from the ground truth with random noises. The statistics of the results were performed. As shown in Table III, the effect of the background noise on the PIV results mainly contributes to the random measurement errors, and the three methods are approximately equally affected by the noise when the SNR is very small (i.e., SNR ≈ 3).

B. Initial condition of the optimization: Adaptive window size

The optimization method gives local optimization in parameter space, and the initial guess is essential to the optimization result. The PIV tracers are assumed to be seeded homogeneously in space. The seeding is not locally uniform in space so a conservative relative large window is needed to include a sufficient number of tracers (to faithfully capture the local flow motion). An interrogation window that includes several tracers is preferentially used, and the drawback is that small flow structures cannot be resolved. When a small interrogation window is used, it may include a few tracers in some windows or maybe no tracer in other windows. These inherent characteristics of the tracer seeding result in scattered noise on the vector field, when a small interrogation window is used, even with spatial smoothing in the global optimization (see Fig. 3).

The concept of adaptive window size can be used to optimize the number of tracers in an interrogation window to suppress the noise and improve the measurement accuracy (Theunissen *et al.*, 2007; 2010). The method of the adaptive window was examined here for the preparation of an initial velocity field for the optimization process.

This test was performed with the synthetic image pair from the PIV Challenge (Stanislas *et al.*, 2008). The images are of 1000×1000 pixels^2 (part of the PIV Challenge images) and present sets of vortices that have a wide range of sizes [approximately seven sizes as visually read in Fig. 7(a)]. The same image pair was processed by the classic and the global optimization method, with the interrogation window of 32×32 pixels^2 (the neighboring vector distance is eight pixels) and
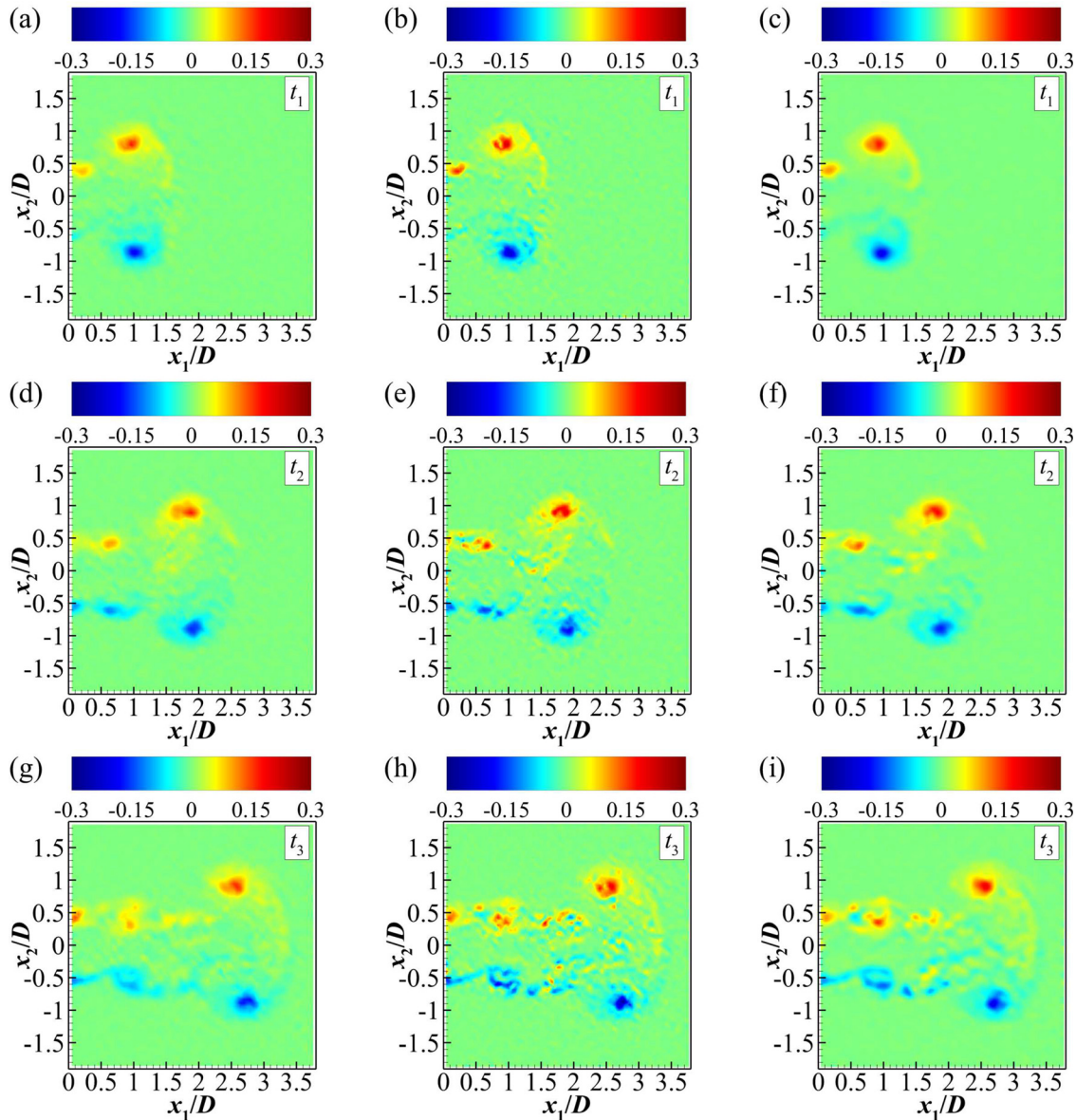
FIG. 5. Instantaneous vorticity maps obtained with the classical PIV method, the global optimization method, and the present method. Three rows correspond to the results at three time instants, from t_1 to t_3. Column (a), (d), and (g) corresponds to the result of the classic PIV in a window size of 32×32 pixels^2. Column (b), (e), and (h) corresponds to the global optimization method in a window size of 24×24 pixels^2, and (c), (f), (i) for the present method in a window size of 24×24 pixels^2. The window overlap is 50% for all panels. Multimedia view: https://doi.org/10.1063/5.0091839.2

5×5 pixels^2 (the neighboring vector distance is three pixels), respectively. The classic method gives very good velocity measurements for the large vortices and smears out the vortices in small sizes due to the use of the 32×32 pixels^2 window, as expected. The global optimization method captures large and small vortices (benefited by the small window of 5×5 pixels^2) and only misses the very small ones, where the displacements are sub-pixels in magnitude. Nevertheless, the velocity field is contaminated with noticeable noises, even for the very large vortices, due to the use of a small interrogation window. For obtaining

adaptive sized interrogation windows, the classic PIV algorithm is used to obtain five displacement fields with interrogation windows of 5×5, 8×8, 16×16, 24×24, and 32×32 pixels^2, respectively, while the neighboring vector distance remains to be three pixels. At each vector position, the coefficient of cross correlation is found to approximately vary with the window size, as shown in Fig. 8(a). At each vector position, the window size corresponding to the maximum correlation of the cross correlation is taken as the optimal window size. As shown in Fig. 8(b), the distribution of the optimized window sizes captures
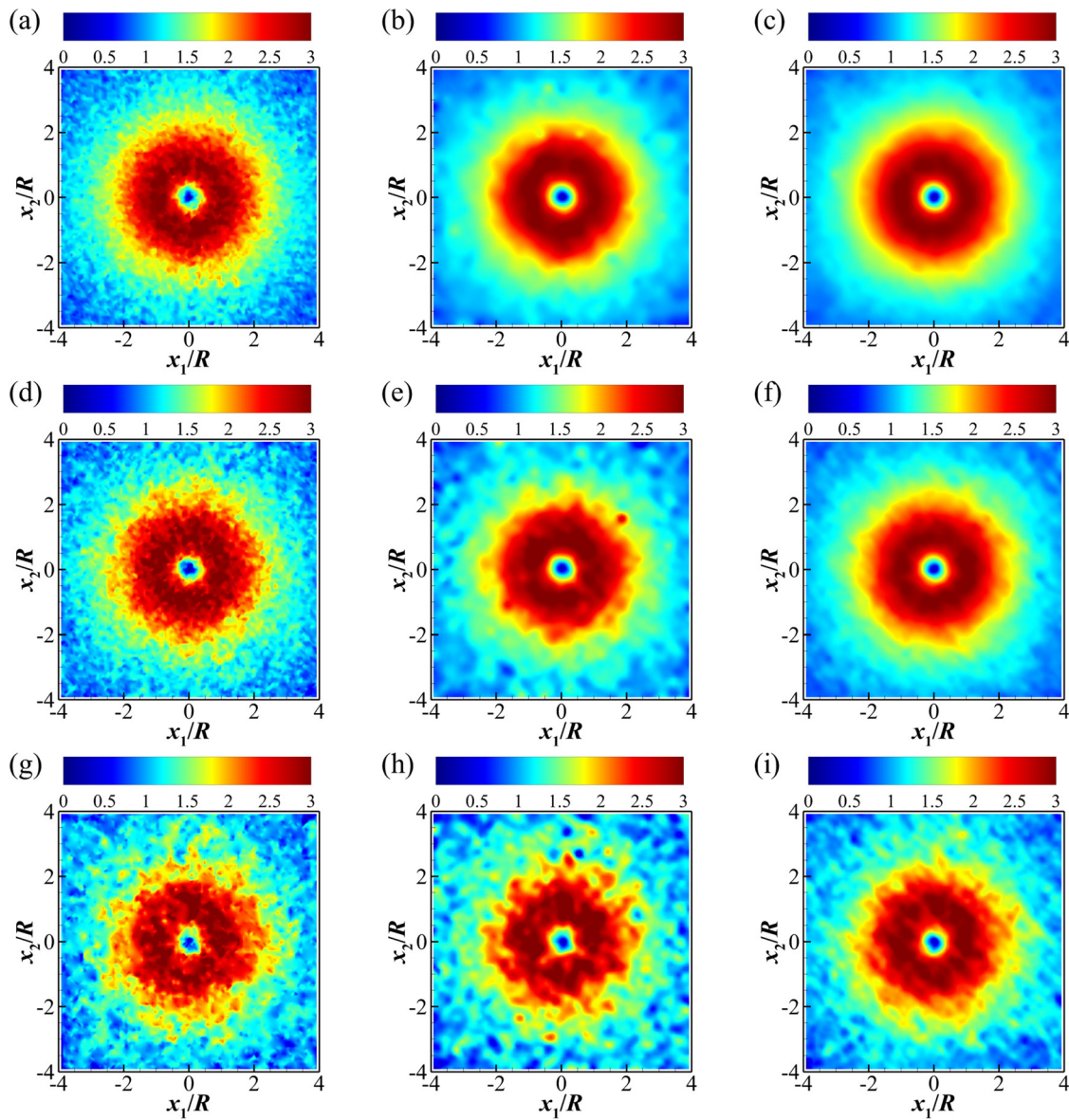
FIG. 6. The contours of the velocity v_θ obtained from tracer images with superimposed random noises: (a), (d), and (g) the classical PIV method, (b), (e), and (h) the global optimization PIV method, and (c), (f), and (i) the spatiotemporal optimization PIV method. The signal-to-noise ratio is 12.30 (a)–(c), 6.15 (d)–(f), and 3.07 (g)–(i). They are from the same time instant (the same time as Fig. 3).

the characteristics of the vortex patterns, given that the smaller window sizes are preferred for smaller vortices, while for larger ones, the larger window sizes are preferred.

The above test suggests that the initial velocity field prepared with the adaptive window method may give a better result than the spatiotemporal optimization method. To examine this, the synthetic tracer images were generated that the imposed velocity field takes the analogical form as in Stanislas et al. (2008). As shown in Fig. 9, there are four consecutive regions in the image, where each region is occupied by an array of vortices in diameter of 200, 100, 50, and 25 pixels

from left to right. Correspondingly, the tangential velocity of the vortices is 2.5, 2, 1.5, and 1 pixels for the given time interval. Twenty consecutive synthetic images were generated that the imposed velocity field is temporally constant. The set of entire images (800×200 pixels^2) is processed with an interrogation window size of 5×5, 32×32 pixels^2 and the adaptive sizes, as demonstrated in Figs. 9(a)–9(c), respectively. They are used as the initial velocity fields for the spatiotemporal optimization process. The measurement error [defined in Eq. (4)] was evaluated, and the time series of the measurement error is shown in Fig. 10. The systematic measurement error is around 0.3

TABLE III. The systematic and random errors of the PIV measurements from 100 tracer images superimposed with random noises for the Batchelor vortex analogy flow.

Error type	Signal-to-noise ratio	Classic	Global optimization	Spatiotemporal optimization
Systematic	12.30	−0.000 125	−0.0061	0.000 31
Random		0.12	0.076	0.051
Systematic	6.15	0.0026	−0.0022	0.0016
Random		0.17	0.11	0.10
Systematic	3.07	−0.018	0.0060	0.0051
Random		0.23	0.22	0.22

pixels for the initial velocity field prepared with the adaptive windows, smaller than the other two cases (around 0.7 pixels).

VI. CONCLUSION

Improving spatial resolution of velocity measurement can benefit by offering insights into flow physics. In this paper, we propose a PIV algorithm to retrieve the velocity fields in high spatial resolution from the time series of the tracer images. This method minimizes the combination of the residual of the normalized cross-correlation term, a component for spatial smoothness, and a component for temporal smoothness. The component controlling the spatial smoothness is inspired by the optical flow method and is the same as used by Wang *et al.* (2020). The component controlling the temporal smoothness is inspired by the fundamental algorithm of particle tracking velocimetry that the track with the minimum change of the tracer material acceleration over the candidate tracks is taken as the measurement trajectory of a tracer.

The performance of the present method is examined on the synthetic tracer images from the direct numerical simulations of homogeneous isotropic turbulence, Batchelor vortex, and sinusoidal vortex by comparing with that of a classic cross-correlation method and that of the global optimization method. These tests show that the present method gives better results over a time series recording. The present method was applied to PIV measurements of vortex rings in a laboratory experiment. The present method provides better results, given that the noise in the velocity field is suppressed, while more small-scale flow structures can be better captured. Thereafter, the effect of
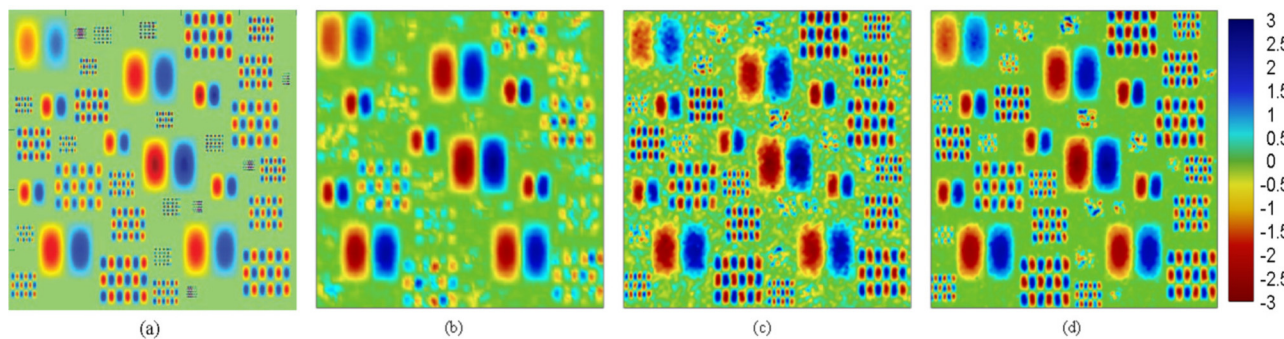

FIG. 7. The contours of the velocity component v: (a) the ground truth [adapted from the PIV challenge (Stanislas *et al.*, 2008) for easy visual comparison], (b) the classical PIV method (with 32×32 pixels^2 interrogations, 75% window overlap), (c) the global optimization PIV method (with 5×5 pixels^2 interrogation window, 60% overlap), and (d) the spatiotemporal optimization PIV method (with adaptive sized windows ranging between 5×5 and 32×32 pixel^2), respectively.
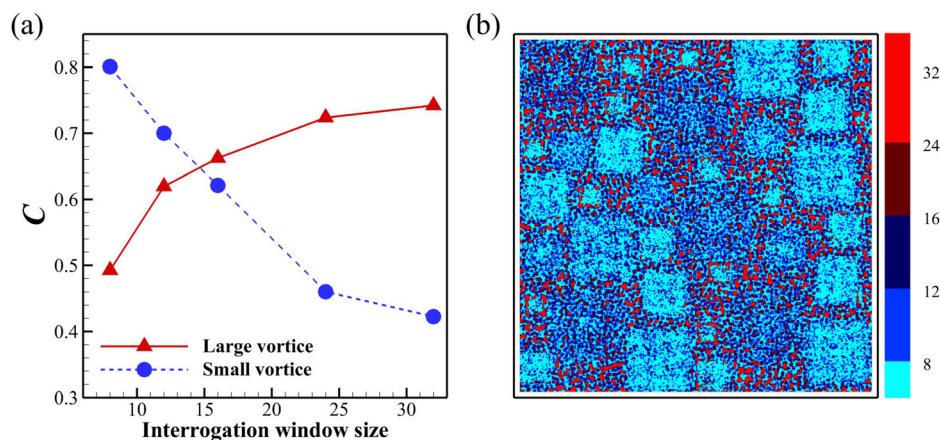

FIG. 8. (a) The coefficient of cross correlation against the interrogation window sizes at two vector positions; and (b) the contours of the optimized window sizes in terms of giving the maximum correlation coefficient at each vector position.
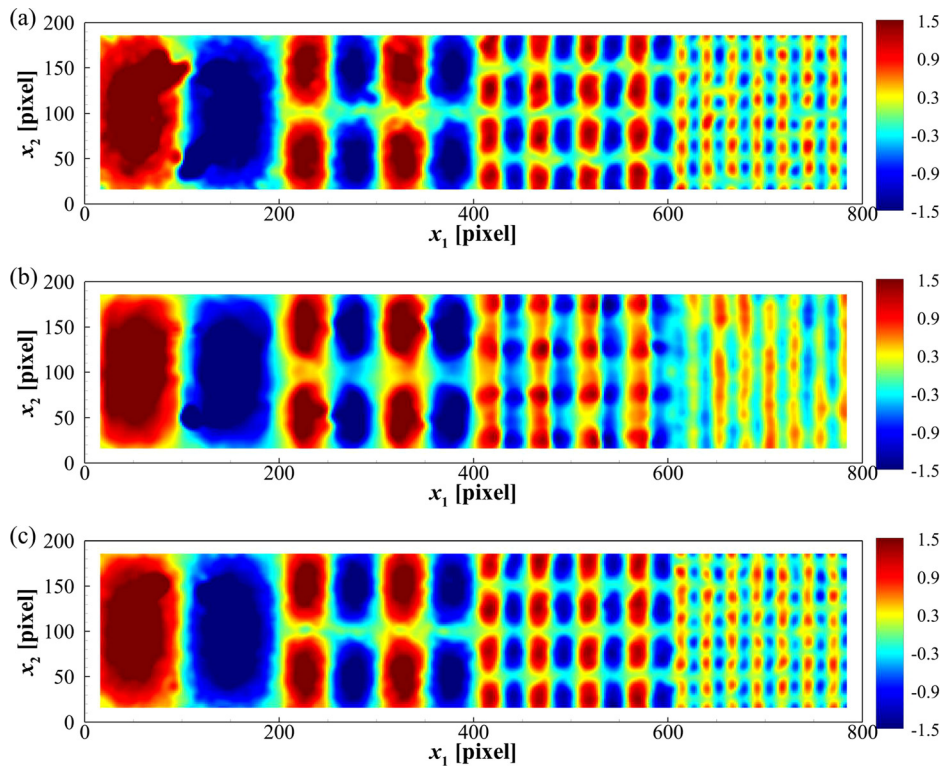
FIG. 9. The initial velocity fields (component v) for the spatiotemporal optimization method: (a) the interrogation window size of five pixels; (b) the interrogation window size of 32 pixels; (c) the adaptive window size (adaptively chosen from 5×5, 8×8, 16×16, 24×24, and 32×32 pixels^2).

the image background noise and that of the initial condition is examined and discussed. For the flows with a wide length scale range of featured flow structures, the initial velocity with adaptively chosen window sizes is found to provide better results for the spatiotemporal optimization method. The high-speed PIV system can capture the PIV images in an approximately time-resolved manner, and it is ideal for use of the proposed method. For the recording in an insufficient sampling rate, the time derivative of the velocity field may largely differ from the truth, so the proposed method may not be applicable.

AUTHOR DECLARATIONS
Conflict of Interest

The authors have no conflicts to disclose.

DATA AVAILABILITY

The data that support the findings of this study are available from the corresponding authors upon reasonable request.

APPENDIX: JACOBIAN MATRIX IN THE OPTIMIZATION METHOD

The Jacobian matrix in the spatiotemporal optimization method is shown in Eq. (A1). The (u, v) in $\mathbf{J}$ is updated every iteration step,
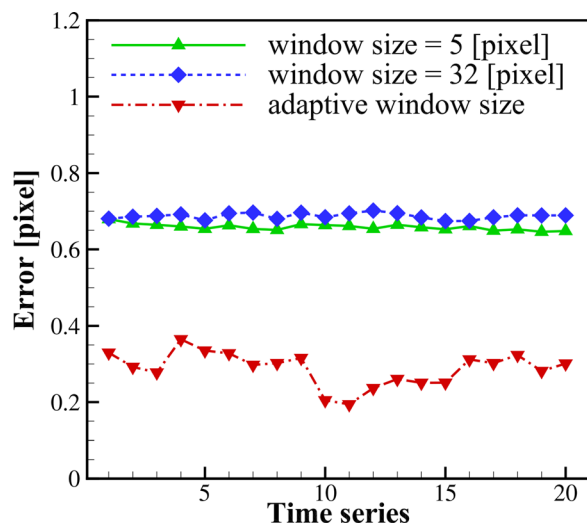

FIG. 10. The time series of the velocity error is with the initial velocity field obtained with an interrogation window sizes of 5, 32, and adaptive sizes (as exampled in Fig. 9).

$$\mathbf{J} = \begin{pmatrix} \mathbf{R}_{cs} & \mathbf{0} & \mathbf{0} \\ \mathbf{0} & \mathbf{R}_{cs} & \mathbf{0} \\ \mathbf{0} & \mathbf{0} & \mathbf{R}_{cs} \\ \mathbf{R}_{-t} & \mathbf{R}_{\delta t} & \mathbf{R}_t \end{pmatrix}, \tag{A1}$$

where $\mathbf{0}$ denotes the 3×2 matrix of zeros, and

$$\mathbf{R}_{cs} = \begin{pmatrix} -\partial C/\partial u & -\partial C/\partial v \\ \alpha_x(D_{xx} + D_{yy}) & 0 \\ 0 & \alpha_y(D_{xx} + D_{yy}) \end{pmatrix}, \tag{A2}$$

$$\mathbf{R}_{-t} = \begin{pmatrix} 1/\delta t - (uD_x + vD_y)/2 & 0 \\ 0 & 1/\delta t - (uD_x + vD_y)/2 \end{pmatrix}, \tag{A3}$$

$$\mathbf{R}_{\delta t} = \begin{pmatrix} -2/\delta t & 0 \\ 0 & -2/\delta t \end{pmatrix}, \tag{A4}$$

$$\mathbf{R}_t = \begin{pmatrix} 1/\delta t + (uD_x + vD_y)/2 & 0 \\ 0 & 1/\delta t + (uD_x + vD_y)/2 \end{pmatrix}. \tag{A5}$$

REFERENCES

Adrian, R. J., "Particle-imaging techniques for experimental fluid mechanics," Annu. Rev. Fluid Mech. **23**, 261–304 (1991).

Arzani, A., Wang, J., and D'Souza, R. M., "Uncovering near-wall blood flow from sparse data with physics-informed neural networks," Phys. Fluids **33**, 071905 (2021).

Batchelor, G. K., "Axial flow in trailing line vortices," J. Fluid Mech. **20**, 645–658 (1964).

Cowen, E. A., and Monismith, S. G., "A hybrid digital particle tracking velocimetry technique," Exp. Fluids **22**, 199–211 (1997).

Deng, Z., He, C., Liu, Y., and Kim, K. C., "Super-resolution reconstruction of turbulent velocity fields using a generative adversarial network-based artificial intelligence framework," Phys. Fluids **31**, 125111 (2019).

Gao, Q., Lin, H., Tu, H., Zhu, H., Wei, R., Zhang, G., and Shao, X., "A robust single-pixel particle image velocimetry based on fully convolutional networks with cross-correlation embedded," Phys. Fluids **33**, 127125 (2021).

Gharib, M., Rambod, E., and Shariff, K., "A universal time scale for vortex ring formation," J. Fluid Mech. **360**, 121–140 (1998).

Glezer, A., "The formation of vortex rings," Phys. Fluids **31**, 3532 (1988).

Keane, R. D., Adrian, R. J., and Zhang, Y., "Super-resolution particle imaging velocimetry," Meas. Sci. Technol. **6**, 754–768 (1995).

Li, S., He, C., and Liu, Y., "A data assimilation model for wall pressure-driven mean flow reconstruction," Phys. Fluids **34**, 015101 (2022).

Liu, B., Tang, J., Huang, H., and Lu, X.-Y., "Deep learning methods for super-resolution reconstruction of turbulent flows," Phys. Fluids **32**, 025105 (2020).

Liu, T., Merat, A., Makhmalbaf, M. H., Fajardo, C., and Merati, P., "Comparison between optical flow and cross-correlation methods for extraction of velocity fields from particle images," Exp. Fluids **56**, 166 (2015).

Liu, T., and Shen, L., "Fluid flow and optical flow," J. Fluid Mech. **614**, 253–291 (2008).

Ma, X., Gong, X., and Jiang, N., "Experimental study of vortex formation in pulsating jet flow by time-resolved particle image velocimetry," Phys. Fluids **34**, 035105 (2022).

Malik, N. A., Dracos, T., and Papantoniou, D. A., "Particle tracking velocimetry in three-dimensional flows. Part II: Particle tracking," Exp. Fluids **15**, 279–294 (1993).

Morimoto, M., Fukami, K., and Fukagata, K., "Experimental velocity data estimation for imperfect particle images using machine learning," Phys. Fluids **33**, 087121 (2021).

Raffel, M., Willert, C. E., Scarano, F., Kähler, C. J., Wereley, S. T., and Kompenhans, J., Particle Image Velocimetry: A Practical Guide (Springer, 2018).

Scarano, F., "A super-resolution particle image velocimetry interrogation approach by means of velocity second derivatives correlation," Meas. Sci. Technol. **15**, 475–486 (2004).

Scarano, F., and Riethmuller, M. L., "Advances in iterative multigrid PIV image processing," Exp. Fluids **29**, S051–S060 (2000).

Scarano, F., and Riethmuller, M. L., "Iterative image deformation methods in PIV," Meas. Sci. Technol. **13**, R1–R19 (2002).

Schanz, D., Gesemann, S., and Schröder, A., "Shake-The-Box: Lagrangian particle tracking at high particle image densities," Exp. Fluids **57**, 70 (2016).

Schneiders, J. F. G., Scarano, F., and Elsinga, G. E., "Resolving vorticity and dissipation in a turbulent boundary layer by tomographic PTV and VIC+," Exp. Fluids **58**, 27 (2017).

Sciacchitano, A., Scarano, F., and Wieneke, B., "Multi-frame pyramid correlation for time-resolved PIV," Exp. Fluids **53**, 1087–1105 (2012).

Stanislas, M., Okamoto, K., Kähler, C. J., Westerweel, J., and Scarano, F., "Main results of the third international PIV challenge," Exp. Fluids **45**, 27–71 (2008).

Stitou, A., and Riethmuller, M. L., "Extension of PIV to super resolution using PTV," Meas. Sci. Technol. **12**, 1398–1403 (2001).

Theunissen, R., Scarano, F., and Riethmuller, M. L., "An adaptive sampling and windowing interrogation method in PIV," Meas. Sci. Technol. **18**, 275–287 (2007).

Theunissen, R., Scarano, F., and Riethmuller, M. L., "Spatially adaptive PIV interrogation based on data ensemble," Exp. Fluids **48**, 875–887 (2010).

Wang, H., He, G., and Wang, S., "Globally optimized cross-correlation for particle image velocimetry," Exp. Fluids **61**, 228 (2020).

Wang, H., Liu, Y., and Wang, S., "Dense velocity reconstruction from particle image velocimetry/particle tracking velocimetry using a physics-informed neural network," Phys. Fluids **34**, 017116 (2022).

Wang, H., Yang, Z., Li, B., and Wang, S., "Predicting the near-wall velocity of wall turbulence using a neural network for particle image velocimetry," Phys. Fluids **32**, 115105 (2020).

Westerweel, J., "Fundamentals of digital particle image velocimetry," Meas. Sci. Technol. **8**, 1379–1392 (1997).

Xu, D., and Chen, J., "Accurate estimate of turbulent dissipation rate using PIV data," Exp. Therm. Fluid Sci. **44**, 662–672 (2013).

Xu, H., "Tracking Lagrangian trajectories in position-velocity space," Meas. Sci. Technol. **19**, 075105 (2008).

Xu, H., Zhang, W., and Wang, Y., "Explore missing flow dynamics by physics-informed deep learning: The parameterized governing systems," Phys. Fluids **33**, 095116 (2021).